

Article

Low-Pressure Plasma-Processed NiCo Metal–Organic Framework for Oxygen Evolution Reaction and Its Application in Alkaline Water Electrolysis Module

Yu-Lun Su ^{1,2}, Shuo-En Yu ^{2,3}, I-Chih Ni ⁴, Chih-I Wu ^{3,4}, Yong-Song Chen ⁵ , Yi-Cheng Chuang ⁵, I-Chun Cheng ⁴ 
and Jian-Zhang Chen ^{1,2,3,*} 

- ¹ Graduate Institute of Applied Mechanics, National Taiwan University, Taipei City 10617, Taiwan; r11543032@ntu.edu.tw
 - ² Advanced Research Center for Green Materials Science and Technology, National Taiwan University, Taipei City 10617, Taiwan; f11k45004@ntu.edu.tw
 - ³ Graduate School of Advanced Technology, National Taiwan University, Taipei City 10617, Taiwan; chihiwu@ntu.edu.tw
 - ⁴ Graduate Institute of Photonics and Optoelectronics and Department of Electrical Engineering, National Taiwan University, Taipei City 10617, Taiwan; ichihni@ntu.edu.tw (I.-C.N.); iccheng@ntu.edu.tw (I.-C.C.)
 - ⁵ Department of Mechanical Engineering and Advanced Institute of Manufacturing with High-Tech Innovations, National Chung Cheng University, Chiayi County 621301, Taiwan; imeysc@ccu.edu.tw (Y.-S.C.); yicheng@ccu.edu.tw (Y.-C.C.)
- * Correspondence: jchen@ntu.edu.tw

Abstract: Ar, Ar/H₂ (95:5), and Ar/O₂ (95:5) plasmas are used for treating the NiCo metal–organic framework (MOF), and the plasma-processed NiCo MOF is applied for catalyzing the oxygen evolution reaction (OER) in a 1 M KOH electrolyte. Linear sweep voltammetry measurements show that after plasma treatment with Ar/H₂ (95:5) and Ar gases, the overpotential reaches 552 and 540 mV, respectively, at a current density of 100 mA/cm². The increase in the double-layer capacitance further confirms the enhanced oxygen production activity. We test the Ar plasma-treated NiCo MOF as an electrocatalyst at the OER electrode and Ru as an electrocatalyst at the hydrogen evolution reaction (HER) electrode in the alkaline water electrolysis module. The energy efficiency of the electrolyzer with the Ar plasma-processed NiCo-MOF catalyst increases from 54.7% to 62.5% at a current density of 500 mA/cm² at 25 °C. The alkaline water electrolysis module with the Ar plasma-processed catalyst also exhibits a specific energy consumption of 5.20 kWh/m³ and 4.69 kWh/m³ at 25 °C and 70 °C, respectively. The alkaline water electrolysis module performance parameters such as the hydrogen production rate, specific energy consumption, and energy efficiency are characterized at temperatures between 25 °C and 70 °C. Our experimental results show that the NiCo MOF is an efficient OER electrocatalyst for the alkaline water electrolysis module.

Keywords: NiCo; metal–organic framework (MOF); oxygen evolution reaction (OER); plasma; electrocatalyst; alkaline water electrolysis



Citation: Su, Y.-L.; Yu, S.-E.; Ni, I.-C.; Wu, C.-I.; Chen, Y.-S.; Chuang, Y.-C.; Cheng, I.-C.; Chen, J.-Z. Low-Pressure Plasma-Processed NiCo Metal–Organic Framework for Oxygen Evolution Reaction and Its Application in Alkaline Water Electrolysis Module. *J. Compos. Sci.* **2024**, *8*, 19. <https://doi.org/10.3390/jcs8010019>

Academic Editors: Francesco Tornabene and Thanasis Triantafyllou

Received: 8 November 2023

Revised: 20 December 2023

Accepted: 2 January 2024

Published: 7 January 2024



Copyright: © 2024 by the authors. Licensee MDPI, Basel, Switzerland. This article is an open access article distributed under the terms and conditions of the Creative Commons Attribution (CC BY) license (<https://creativecommons.org/licenses/by/4.0/>).

1. Introduction

Hydrogen energy is a type of green energy that is considered a highly promising alternative to fossil energy [1–5]. Compared to other energy sources such as gasoline and coal, hydrogen has a higher energy density and its combustion only produces water, without emitting greenhouse gases like carbon dioxide [6–9]. Developing hydrogen as an alternative fuel could reduce the reliance on fossil fuels, and therefore, hydrogen is commonly being used in fuel cells and, more recently, in hydrogen-powered vehicles worldwide [10–12].

An alkaline water electrolysis system can be used for electrolytic hydrogen production [13–16]. In this system, the oxygen evolution reaction (OER) and hydrogen evolution reaction (HER) occur simultaneously at the anode and cathode, respectively. A theoretical voltage of 1.23 V is required between the anode and cathode to drive these reactions, and an additional overpotential is applied to facilitate the reactions. Electrocatalysts play a crucial role in reducing the overpotential by promoting water reactions in the HER or OER. Although metals such as Ir and Pt exhibit high electrocatalytic efficiency, they are expensive [17–20]. Studies have explored alternatives and found that transition metals such as nickel and cobalt exhibit good catalytic activity toward the OER [21,22]; advantageously, transition metal-based oxides are inexpensive, easy to synthesize, and environmentally friendly [23–25].

Metal–organic frameworks (MOFs) are unique artificial materials composed of metal ions (or metal clusters) and organic linkers [26,27]. They have a high surface area, excellent adsorption capacity, and tunable pore sizes [28–30]. MOFs have an adjustable structure and exhibit diverse functionalities, making them commonly used as catalysts [31]. MOFs can be transformed into oxides, phosphides, sulfides, selenides, carbides, etc., to enhance their electrocatalytic activity and stability [32–34]. Among these, nickel-based OER catalysts, including those in hydroxide [35], sulfide [36], and phosphide [37] forms, exhibit superior OER catalytic activity under alkaline conditions. In particular, bimetallic cobalt- and nickel-based compounds show enhanced catalytic performance [38]. For instance, Guan and co-workers achieved improved catalytic performance of NiCo MOF/NF by incorporating sulfur through sulfidation [39].

Plasma treatment is a simple and scalable method for modifying metal surfaces [40–42]. Studies have shown that vacancies and defects can be introduced in materials to modulate their surface electronegativity, charge concentration, and redistribution, and to thereby influence their catalytic performance [43,44]. Argon (Ar) and hydrogen (H₂) plasma treatments have similar effects [45–48]. For example, Wang et al. performed Ar plasma bombardment of Co₃O₄ to introduce abundant oxygen vacancies on its surface; this created plasma-etched Co₃O₄ nanosheets with increased exposed surface area [49]. Oxygen vacancies can adjust the oxidation state of the metal and increase the number of active sites, thus significantly affecting the OER activity [50,51].

In this study, NiCo MOF was tested as an OER electrocatalyst in an alkaline water environment. NiCo MOF was treated with Ar, Ar/H₂ (95:5), and Ar/O₂ (95:5) plasmas to create more electrocatalytic active sites on its surface. The plasma-treated NiCo MOF was then used in an anion exchange membrane alkaline water electrolysis module. Electrochemical characterization of the alkaline water electrocatalyst with Ar plasma-processed NiCo-MOF electrocatalyst was performed between 25 °C and 70 °C.

2. Experimental

2.1. Synthesis of NiCo-MOF/NF Electrocatalyst

Nickel foam (NF) with a thickness of 1.7 mm was purchased from HOMOYTECH. The untreated or original NF was cut into rectangular pieces measuring 3 cm × 1 cm. Subsequently, it was sequentially sonicated for 20 min in 0.1 M H₂SO₄ solution, deionized (DI) water, alcohol, and acetone to remove the oxide layer on its surface; the resulting NF is called NF@. Then, NiCo MOFs/NF@ was prepared using a solvothermal method. First, 1 mmol of Ni(NO₃)₂·6H₂O, 1 mmol of Co(NO₃)₂·6H₂O, 2 mmol of terephthalic acid, and 37.5 mL of ethanol were mixed and stirred continuously for 30 min. Then, NF@ was placed in a Teflon autoclave reactor and kept in an oven at 130 °C for 7 h. After cooling, it was removed and rinsed with DI water, and then dried in an oven at 60 °C for 10 min to obtain NiCo MOFs/NF@. Finally, the electrode was treated with low-pressure plasma using 100% Ar, 95% Ar + 5% H₂, and 95% Ar + 5% O₂ gases for 1 min. The corresponding electrocatalysts were referred to as NiCo MOFs/NF@-Ar, NiCo MOFs/NF@-AH, and NiCo MOFs/NF@-AO, respectively. Figure 1 illustrates the sample preparation procedure.

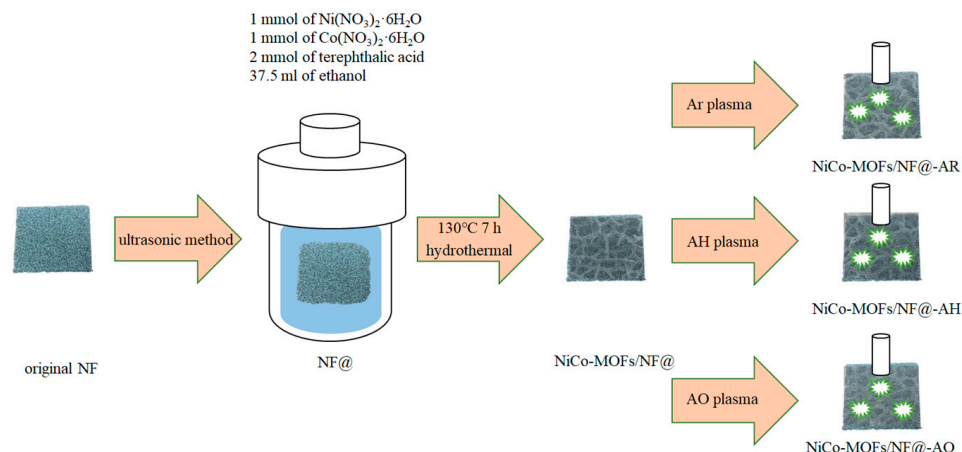


Figure 1. Synthesis of NiCo MOFs/NF@.

2.2. Synthesis of NiCo/CP and Ru/CP Electrocatalyst

To make the NiCo MOF suitable for use in an anion exchange membrane alkaline water electrolysis module, we similarly grew the NiCo MOF on carbon paper as the anode catalyst by using a solvothermal method. The carbon paper was cut into a $5 \text{ cm} \times 5 \text{ cm}$ square (thickness: 0.35 mm, CeTech) and cleaned by exposing it to a plasma of 95% Ar + 5% O_2 gas for 1 min. Next, a mixture of 4 mmol of $\text{Ni}(\text{NO}_3)_2 \cdot 6\text{H}_2\text{O}$, 4 mmol of $\text{Co}(\text{NO}_3)_2 \cdot 6\text{H}_2\text{O}$, 8 mmol of terephthalic acid, and 150 mL of ethanol was prepared and stirred continuously for 30 min. The carbon paper was then placed in a high-pressure autoclave and heated in an oven at $130 \text{ }^\circ\text{C}$ for 7 h. After cooling, the samples were rinsed with deionized (DI) water and dried in the oven at $60 \text{ }^\circ\text{C}$. These samples were referred to as NiCo/CP. Lastly, low-pressure plasma treatment was performed using 100% Ar for 1 min to produce NiCo/CP-Ar.

For the cathode catalyst, carbon paper of the same dimensions ($5 \text{ cm} \times 5 \text{ cm}$) was used. It was pre-cleaned by exposing it to a plasma of 95% Ar + 5% O_2 gas for 1 min. Then, a solution containing 5 mmol of $\text{RuCl}_3 \cdot 3\text{H}_2\text{O}$, 80 mL of ethylene glycol, and 80 mL of DI water was added to the high-pressure autoclave and stirred continuously for 30 min. Subsequently, the carbon paper was placed in the high-pressure autoclave and heated in an oven at $130 \text{ }^\circ\text{C}$ for 7 h. After cooling, the samples were rinsed with DI water and dried in the oven at $60 \text{ }^\circ\text{C}$. These samples were referred to as Ru/CP.

2.3. Anion Exchange Membrane Alkaline Water Electrolysis Module

Our alkaline water electrolysis system is a symmetrical device with an anode and a cathode reaction zone. Figure 2 shows its components. From the outermost layer to the innermost layer, it includes an aluminum plate, a polypropylene gasket, gold-plated copper electrode plates, flexible graphite sheets, VITON a graphite flow plate, rubber gasket, and a self-made electrocatalyst. A $6 \text{ cm} \times 6 \text{ cm}$ anion exchange membrane (Sustainion[®] X37-50 grade RT membrane, Dioxide Materials, Boca Raton, FL, USA) is placed at the interface between the anode and cathode to separate them. The X37-50 membrane needs to be soaked in 1 M KOH for 24 h before use for activation. The system was tested at room temperature with a flow rate of 10 mL/min of 1 M KOH supplied to the anode and cathode through two peristaltic pumps. The heating system consists of two heating patches ($60 \times 67 \text{ mm}$, 24 V, 40 W) attached to both sides of aluminum plates. The temperature was controlled using a proportional–integral–derivative temperature controller (DTA4848V1, Delta Electronics, Inc., Taipei City, Taiwan), and the temperature of the graphite flow plate was measured using a K-type thermocouple.

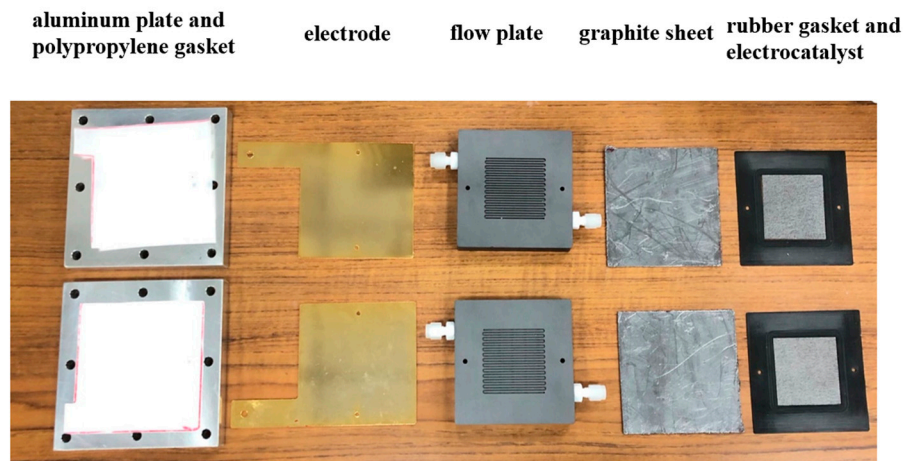


Figure 2. Components of anion exchange membrane alkaline water electrolysis module.

2.4. Material Characterization

The samples were analyzed using various techniques. Scanning electron microscopy (SEM; JEOL JSM-IT100, Tokyo, Japan) was used to examine the morphology and surface structure. X-ray photoelectron spectroscopy (XPS; Thermo Scientific Theta Instrument, Waltham, MA, USA) was used to characterize the chemical compositions. An X-ray diffractometer (XRD; Bruker D2 PHASER, Billerica, MA, USA) with Cu-K α radiation ($\lambda = 1.54060 \text{ \AA}$) was used to perform crystal phase analysis. A goniometer (Sindatek, Model 100SB, Taipei City, Taiwan) was used to measure the water contact angle of the samples. Additionally, a Plasma Cleaner PDC-32G was used to perform low-pressure plasma treatment of the samples with a pressure of 0.6 torr, flow rate of 10 sccm, and power of 11 W.

2.5. Electrochemical Measurement

We used Autolab (PGSTAT204, Metrohm, Utrecht, The Netherlands) in a three-electrode setup, with Ag/AgCl as the reference electrode, Pt as the counter electrode, and NF as the working electrode, to measure the OER electrocatalytic performance. Cyclic voltammetry (CV; potential scan rate: 20–300 mV/s), linear sweep voltammetry (LSV; scan rate: 5 mV/s), and electrochemical impedance spectroscopy (EIS; 0.1–100,000 Hz) were conducted to measure the performance of the electrocatalyst.

In the LSV measurement, the potential E of the electrode was converted to the corresponding potential relative to the reversible hydrogen electrode (RHE) by using the Nernst equation: $E_{\text{RHE}} = E_{\text{Ag/AgCl}} + 0.059 \times \text{pH} + 0.197$ [52,53], where E_{RHE} is the potential relative to the RHE, and $E_{\text{Ag/AgCl}}$ is the experimentally measured potential relative to the Ag/AgCl reference electrode. The OER performance of the electrocatalyst was evaluated in a 1 M KOH electrolyte, and the overpotential (η) in the OER was calculated by subtracting the standard oxidation potential as $\eta = E_{\text{RHE}} - 1.23$.

3. Results and Discussion

3.1. SEM Results of Electrocatalysts

SEM was used to study the morphology of the electrode surface. Figure 3 shows the SEM images. At a magnification of 70 \times , NF exhibits a porous structure, and small protruding particles are attached to the framework after NiCo deposition. At a magnification of 3000 \times , NiCo MOF appears to be layered, and branching is observed on the surface after plasma treatment. The increased surface area and surface oxygen vacancies make a significant contribution to the excellent electrocatalytic performance in the OER [49].

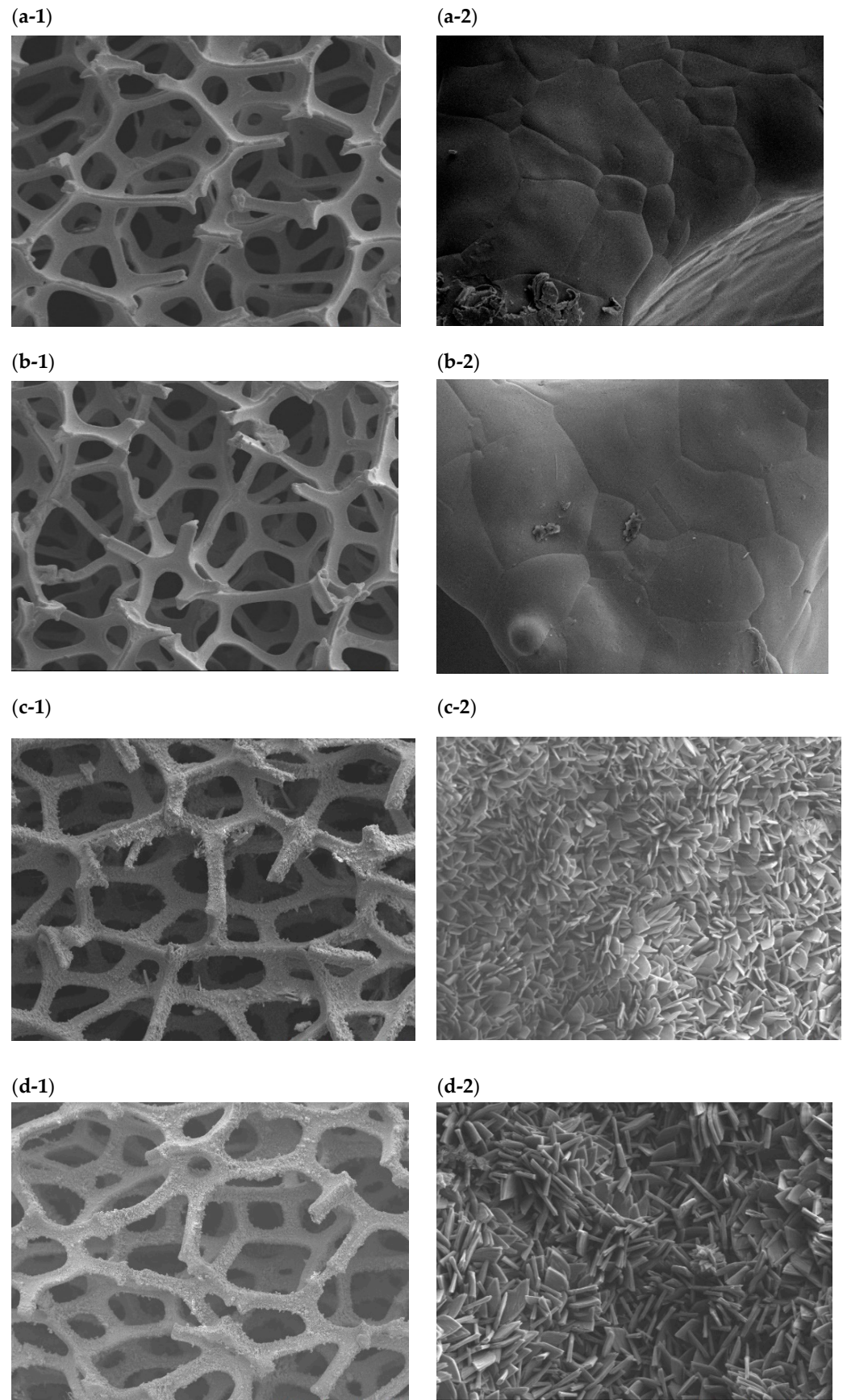


Figure 3. Cont.

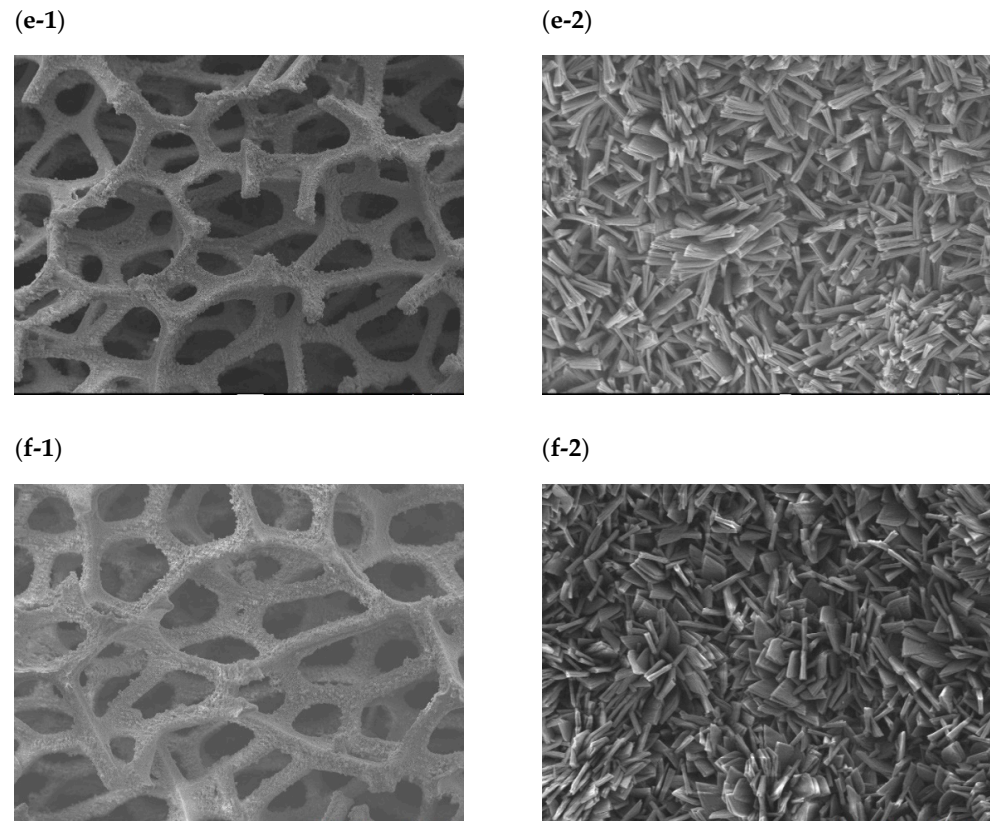


Figure 3. SEM images with 70 \times and 3000 \times magnification: (a-1,a-2) original NF, (b-1,b-2) NF@, (c-1,c-2) NiCo MOFs/NF@, (d-1,d-2) NiCo MOFs/NF@-Ar, (e-1,e-2) NiCo MOFs/NF@-AH, and (f-1,f-2) NiCo MOFs/NF@-AO.

3.2. Water Contact Angles of Grown Electrocatalysts

The water contact angle is an important indicator for assessing the hydrophilicity of a material. In the OER and HER, the electrolyte comes into contact with the electrocatalyst and infiltrates the electrode surface, thereby increasing the reaction area [54]. Therefore, it is crucial to enhance the hydrophilicity of the electrocatalyst [55]. The hydrophilicity also improves the detachment of the generated gas from the electrocatalysts. Figure 4 indicates that the water contact angle on the original NF is 80.01 $^{\circ}$, and the material is relatively less hydrophilic. However, after acid washing, the surface oxides are removed from the NF, thus transforming the originally less hydrophilic surface into a more hydrophilic one. After regrowing NiCo and applying low-pressure plasma treatment, the surface of the electrocatalyst becomes even more hydrophilic, making it beneficial for the OER reaction and bubble detachment and thereby enhancing the water electrolysis performance.

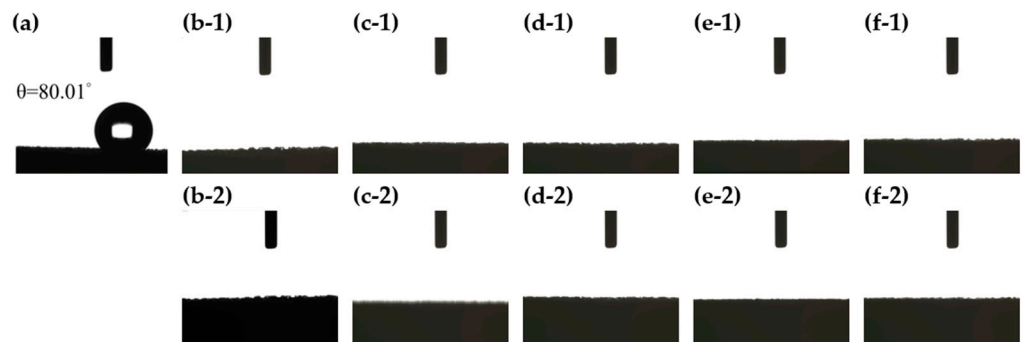


Figure 4. Water contact angles: (a) original NF, (b-1,b-2) NF@, (c-1,c-2) NiCo MOFs/NF@, (d-1,d-2) NiCo MOFs/NF@-Ar, (e-1,e-2) NiCo MOFs/NF@-AH, and (f-1,f-2) NiCo MOFs/NF@-AO.

3.3. XPS and XRD

The electrocatalytic activity of a material can be influenced by its morphological and material characteristics [56]. XRD analysis was conducted to understand the crystal structure of the prepared sample. As shown in Figure 5a, at scanning angles of 20° – 60° , strong peak signals were observed at 45.21° and 52.62° ; these correspond to the (111) and (200) planes of the NF, respectively [48]. These signals indicate the presence of the NF substrate. As shown in Figure 5b, at lower angles with a more precise scanning speed, peaks were observed at 8.85° and 17.83° . These are attributable to the NiCo MOF [39], suggesting that it has grown successfully. In Figure 5b, the XRD peak shifts may be attributed to the non-uniform growth of our material through solvent–thermal synthesis, as not every part is evenly distributed. Additionally, low-pressure plasma treatment may insert atoms or create defects, resulting in a change in the interplanar spacing. However, the peak shifts are not systematic, and more experimental results may be required to understand the real reason for the shifts of XRD peaks.

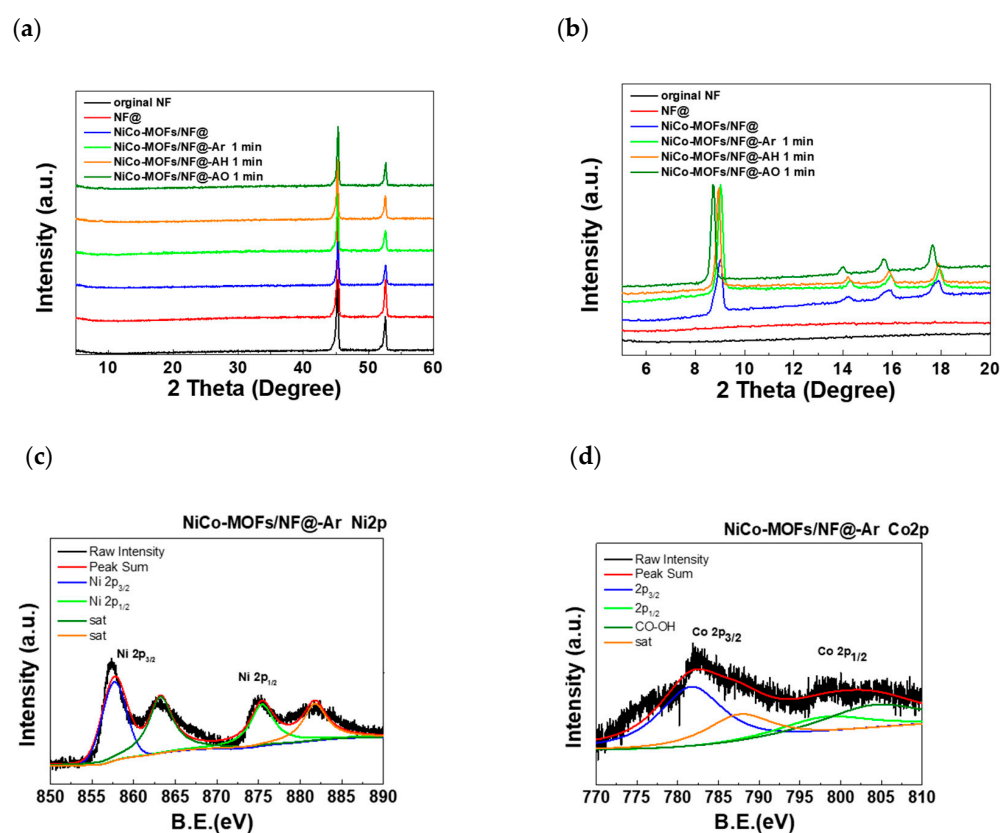


Figure 5. (a) XRD patterns of NF, NF@, NiCo MOFs/NF@, NiCo MOFs/NF@-Ar, NiCo MOFs/NF@-AH, and NiCo MOFs/NF@-AO with 2θ range of 5° – 60° . (b) XRD patterns with 2θ range of 5° – 20° . (c) XPS spectra of Ni 2p and (d) XPS spectra of Co 2p.

XPS measurements were conducted to understand the elemental composition of the prepared samples. Figure 5c shows the four peaks in the Ni2p spectra of NiCo MOFs/NF@-Ar. The Ni2p spectra show characteristic peaks of the Ni^{2+} oxidation state, corresponding to the Ni-O bonds in the MOF structure, with binding energies at 857.4 eV ($2p_{3/2}$). The peak at 875.5 eV ($2p_{1/2}$) is attributed to the Ni-OH bond, and the peaks near 862.6 eV and 882.4 eV are attributed to the satellite peaks of Ni2p [57]. Figure 5d shows four peaks in the Co2p spectra, corresponding to the $\text{Co}2p_{3/2}$ and $\text{Co}2p_{1/2}$ peaks at 782.0 eV and 798.3 eV, respectively. The peak intensities of $\text{Co}2p_{3/2}$ and $\text{Co}2p_{1/2}$ have a ratio of 2:1. The binding energies at 804.4 eV and 787.9 eV are assigned to the Co-OH bond and the satellite peaks of Co2p, respectively [38,58]. More XPS spectra are included in Supplementary Materials.

3.4. Electrochemical Characterization

The OER pathway involves the transfer of four electrons, and each electron transfer requires an energy barrier to be overcome [59–61]. This results in slow kinetics for water electrolysis. Therefore, catalysts that show good activity in the OER are used to reduce the voltage required for water electrolysis closer to the theoretical value of 1.23 V. The overpotential (η) becomes an important indicator in this regard, where a lower overpotential indicates the ability to drive the water oxidation reaction with less energy [62]. The electrocatalytic activity of each sample was measured in a 1 M KOH electrolyte. The OER polarization curves in Figure 6a were obtained through LSV testing. Table 1 lists the electrochemical characterization results. The original NF has an overpotential of 1906 mV at a current density of 100 mA/cm². After depositing the NiCo alloy on the NF, the overpotential decreased significantly. Furthermore, after low-pressure plasma treatment, NiCo MOFs/NF@-Ar and NiCo MOFs/NF@-AH exhibited even lower overpotentials of 540 mV and 552 mV at a current density of 100 mA/cm², respectively. This confirms that plasma treatment can create more active sites, introduce surface defects, and enhance catalytic efficiency. In addition, a distinct oxidation peak is observed around 1.4–1.5 V; it is attributed to Ni²⁺/Ni³⁺ or Co²⁺/Co³⁺ [63], consistent with the XPS analysis results.

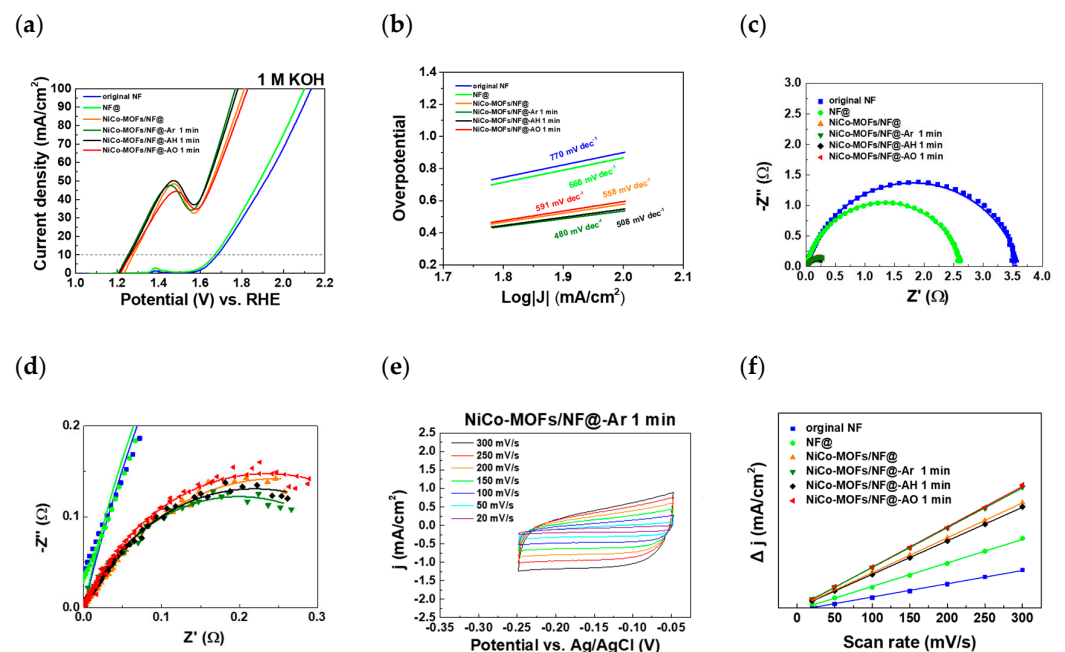


Figure 6. (a) LSV OER polarization curves in 1 M KOH. (b) Tafel Slope plots. (c) Nyquist plots at an overpotential of 400 mV versus RHE. (d) Enlarged figure of Nyquist plots. (e) CV potential curves of NiCo MOFs/NF@-Ar at different scan rates. (f) Electric double-layer capacitance of different electrode materials.

Table 1. Electrochemical testing result of each electrocatalyst.

Sample	Tafel Slope (mV/dec)	Overpotential (mV) at Current Density of 100 mA/cm ²	R _{ct} (Ω)	2C _{dl} (mF/cm ²)
NF	770	1906	3.61	1.7
NF@	668	1871	2.64	3.0
NiCo MOFs/NF@	558	584	0.50	4.5
NiCo MOFs/NF@-Ar 1 min	480	540	0.40	5.1
NiCo MOFs/NF@-AH 1 min	508	552	0.44	4.3
NiCo MOFs/NF@-AO 1 min	591	601	0.47	5.2

As shown in Figure 6b, the calculated Tafel slope is lower for the samples treated with Ar and AH plasmas. A lower Tafel slope indicates a smaller voltage requirement for a tenfold increase in current, resulting in lower energy consumption [64–67]. The NiCo MOF/NF@-Ar exhibits a Tafel slope of 480 mV/dec, indicating a better catalytic performance.

Figure 6c,d show the EIS results of each electrocatalyst at an overpotential of 400 mV. According to the equivalent circuit model, R_{ct} represents the charge transfer resistance, a measure of the difficulty of charge transfer at the electrode–electrolyte interface during the electrode process [68]. A lower charge transfer resistance indicates an easier electrolysis process [69]. The results also demonstrate that the NiCo MOF/NF@-Ar has the lowest R_{ct} value of 0.40 Ω , indicating higher charge transfer ability and better catalytic performance.

The electrochemical active surface area (ECSA) is used to evaluate the electrocatalytic performance of materials [70]. According to previous studies, the double-layer capacitance (C_{dl}) can reflect the number of active sites on the catalyst [71]. C_{dl} was calculated using CV measurements at different scan rates [72]. Figure 6e shows the I-V curves of NiCo MOFs/NF@-Ar at different scan rates, and the results in Figure 6f indicate that the NiCo MOF/NF@-Ar has a larger ECSA that facilitates contact between the electrocatalyst and electrolyte. More CV curves are included in the Supplementary Materials. These electrochemical results demonstrate that plasma treatments with surface oxygen vacancies and high surface area significantly improve the OER performance [49]. Studies have shown that metal oxides subjected to high-energy ion (Ar^+) bombardment can also generate surface oxygen vacancies [51]. Through plasma treatment, metal oxides can be effectively etched to expose more surface sites and selectively remove surface oxygen to create oxygen vacancies [42,73]. Studies have also found that inert gas plasmas (e.g., Ar plasma) cause activation. After activation, the sample immediately comes into contact with monomers without exposure to oxygen or air. Free radicals formed along the activation process act as initiating active sites [74,75].

3.5. Performance of Alkaline Water Electrolyzer

With electrochemical testing and material analysis, we conducted experiments to verify the catalytic effects of the NiCo MOF and the influence of low-pressure plasma treatment. We deposited the NiCo MOF on carbon paper and compared the results with those of untreated samples using NiCo/CP-Ar treated with argon plasma, based on the electrochemical measurements. The OER and HER are closely related and occur simultaneously. Therefore, the key to improving energy efficiency is related to both the anode and cathode catalyst materials [76–80]. Previous electrochemical measurements have shown that the NiCo MOF is suitable as an electrocatalyst for OER at the anode, while ruthenium (Ru) is used for testing at the cathode. The mass loadings of NiCo/CP and Ru/CP are 4.02 mg/cm² and 0.82 mg/cm², respectively.

Figure 7a shows the relationship between the cell voltage and current density. After the deposition of the NiCo MOF, at a current density of 500 mA/cm², a cell voltage of approximately 2.2 V is required. However, after Ar plasma treatment, the cell voltage is reduced to 2.03 V, indicating that Ar plasma can enhance the catalytic performance of the electrocatalyst [45,75].

Furthermore, we tested the performance of NiCo-Ar/CP at different temperatures. The decrease in cell voltage with increasing temperature was attributed to the lower equivalent electrical impedance of the electrolytic cell at higher temperatures [81,82], and the alkaline electrolyte's conductivity increased nearly linearly with temperature [83,84]. Therefore, temperature plays a crucial role in the operation of the water electrolysis cell. Figure 7b shows that the cell voltage decreases with increasing temperature, indicating that higher operation temperatures have a positive impact on efficiency [85]. However, higher operating temperatures may negatively affect the corrosion resistance of electrolytic cell components and the purity of the generated gases. As a result, commercial alkaline water electrolysis cells generally operate at temperatures below 90 °C [86].

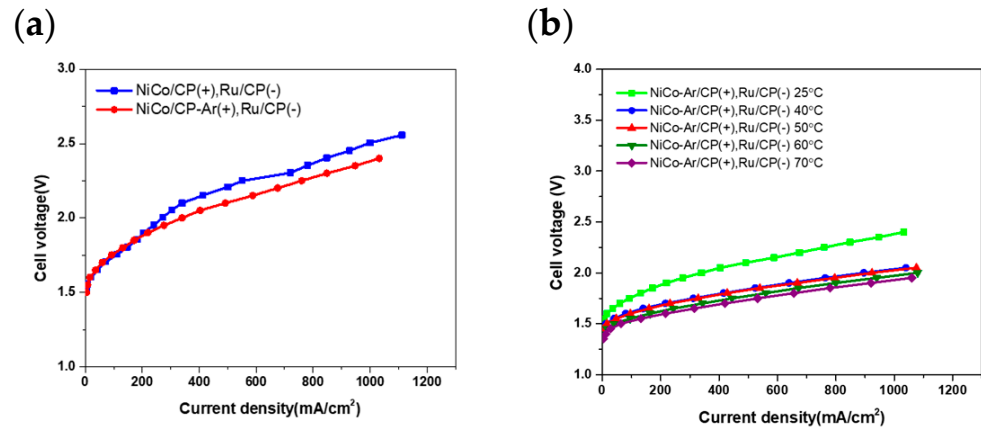


Figure 7. (a) Cell voltage and current density curves in the electrolyzer. NiCo/CP and NiCo/CP-Ar electrocatalysts are compared. (b) Cell voltage–current density of electrolyzers at different temperatures.

Table 2 presents the performance parameters of the electrolyzers at different current densities and different operation temperatures. The energy efficiency (η) is calculated as follows: $\eta = \frac{E_{H_2}}{Q} = \frac{P_{H_2} * 11.7J}{I * V_{ps}}$ [87], where E_{H_2} is the chemical energy of the produced hydrogen gas, Q is the electrical energy input during hydrogen production, P_{H_2} is the amount of hydrogen gas produced in the experiment, 11.7 J is the energy per milliliter of hydrogen gas, I is the current on the electrode, and V_{ps} is the voltage of the power supply. The specific energy consumption for generating a cubic meter of hydrogen gas is also calculated and compared in Table 2. The heating energy is not included in this calculation because heat can be supplied by industrial waste heat or solar heat when generating green hydrogen. After Ar plasma treatment, the energy efficiency at various current densities is improved, thus demonstrating the enhanced catalytic ability and reduced energy loss.

Table 2. Performance of electrolyzers at different current densities and different temperatures.

Electrocatalysts	Current Density	Cell Voltage	Power Supply Voltage	H ₂ production Rate (Experimental)	O ₂ production Rate (Experimental)	Energy Efficiency	Specific Energy Consumption
Unit	mA/cm ²	V	V	mL/min	mL/min	%	kWh/m ³
NiCo/CP(+), Ru/CP(-)	100	1.75	1.84	18	10	76.3	4.26
	500	2.21	2.68	94	49	54.7	5.94
	1000	2.51	3.39	189	52	43.5	7.74
25 °C	100	1.73	1.82	19	10	81.4	3.99
	500	2.03	2.46	98.5	48	62.5	5.20
	1000	2.3	3.16	199	97	49.1	6.62
40 °C	100	1.62	1.71	19	10	86.7	3.75
	500	1.84	2.22	97	50	68.2	4.77
	1000	2.04	2.87	198	101	53.8	6.04
NiCo/CP-Ar(+), Ru/CP(-)	100	1.61	1.66	19.5	10.5	91.6	3.55
	500	1.84	2.25	96.5	50.5	66.9	4.86
	1000	2.03	2.90	196	100	52.7	6.16
60 °C	100	1.56	1.62	19	10.5	91.5	3.55
	500	1.78	2.20	95	51	67.4	4.82
	1000	1.98	2.81	192	101	53.3	6.10
70 °C	100	1.53	1.61	19	10.5	92.0	3.53
	500	1.74	2.16	96	50	69.3	4.69
	1000	1.93	2.78	196	100	55.0	5.91

4. Conclusions

NiCo-MOF catalysts were prepared by using a simple solvothermal method and plasma treatment. Through Ar plasma treatment, the overpotential of NiCo-MOF/NF catalysts was reduced from 584 mV to 540 mV at a current density of 100 mA/cm², indicating improved catalytic performance. This improvement was accompanied by an increase in the ECSA, decrease in charge transfer impedance, and reduction in the Tafel slope, all of which are indicators of enhanced catalytic efficiency. Furthermore, when NiCo-MOF electrocatalysts were applied in an alkaline water electrolysis module, their energy efficiency increased after Ar plasma treatment from 54.7% to 62.5% at a current density of 500 mA/cm² at 25 °C. The alkaline water electrolysis module with the Ar plasma-processed catalyst also exhibited a specific energy consumption of 5.20 kWh/m³ and 4.69 kWh/m³ at 25 °C and 70 °C, respectively. These findings suggest that NiCo is a promising OER catalyst material, and low-pressure plasma treatment enhances its performance; this is consistent with the results obtained from electrochemical measurements.

Supplementary Materials: The following supporting information can be downloaded at: <https://www.mdpi.com/article/10.3390/jcs8010019/s1>, Figure S1. XPS spectra of C1 s; Figure S2. CV potential curves at different scan rates. (a) original NF, (b) NF@, (c) NiCo MOFs/NF, (d) NiCo MOFs/NF@-AH, and (e) NiCo MOFs/NF@-AO.

Author Contributions: Conceptualization, Y.-S.C., I.-C.C. and J.-Z.C.; methodology, Y.-L.S., S.-E.Y., I.-C.N., C.-I.W. and Y.-C.C.; software, Y.-L.S. and S.-E.Y.; validation, Y.-L.S., I.-C.N. and J.-Z.C.; formal analysis, Y.-L.S., S.-E.Y. and I.-C.N.; investigation, Y.-L.S. and I.-C.N.; resources, C.-I.W., Y.-S.C., I.-C.C. and J.-Z.C.; data curation, Y.-L.S. and S.-E.Y.; writing—original draft preparation, Y.-L.S. and J.-Z.C.; writing—review and editing, Y.-L.S. and J.-Z.C.; visualization, Y.-L.S.; supervision, Y.-S.C., I.-C.C. and J.-Z.C.; project administration, Y.-S.C. and J.-Z.C.; funding acquisition, J.-Z.C. All authors have read and agreed to the published version of the manuscript.

Funding: This work was financially supported by the “Advanced Research Center for Green Materials Science and Technology” from the Featured Area Research Center Program within the framework of the Higher Education Sprout Project by the Ministry of Education (MOE) in Taiwan (112L9006). The authors gratefully acknowledge the funding support from the National Science and Technology Council in Taiwan (NSTC) under grant nos. NSTC 111-2221-E-002-088-MY3 and NSTC 112-2218-E-002-050.

Data Availability Statement: Data are contained within the article and supplementary materials.

Conflicts of Interest: The authors declare no conflicts of interest.

References

1. Wang, W.; Xu, X.; Zhou, W.; Shao, Z. Recent progress in metal-organic frameworks for applications in electrocatalytic and photocatalytic water splitting. *Adv. Sci.* **2017**, *4*, 1600371. [[CrossRef](#)] [[PubMed](#)]
2. Cheng, F.; Zhang, T.; Zhang, Y.; Du, J.; Han, X.; Chen, J. Enhancing electrocatalytic oxygen reduction on MnO₂ with vacancies. *Angew. Chem.* **2013**, *125*, 2534–2537. [[CrossRef](#)]
3. Seh, Z.W.; Kibsgaard, J.; Dickens, C.F.; Chorkendorff, I.; Nørskov, J.K.; Jaramillo, T.F. Combining theory and experiment in electrocatalysis: Insights into materials design. *Science* **2017**, *355*, eaad4998. [[CrossRef](#)]
4. Sun, H.; Zhang, W.; Li, J.-G.; Li, Z.; Ao, X.; Xue, K.-H.; Ostrikov, K.K.; Tang, J.; Wang, C. Rh-engineered ultrathin NiFe-LDH nanosheets enable highly-efficient overall water splitting and urea electrolysis. *Appl. Catal. B Environ.* **2021**, *284*, 119740. [[CrossRef](#)]
5. Du, X.; Ma, G.; Zhang, X. Experimental and theoretical understanding on electrochemical activation processes of nickel selenide for excellent water-splitting performance: Comparing the electrochemical performances with M-NiSe (M = Co, Cu, and V). *ACS Sustain. Chem. Eng.* **2019**, *7*, 19257–19267. [[CrossRef](#)]
6. Yu, L.; Lei, T.; Nan, B.; Jiang, Y.; He, Y.; Liu, C. Characteristics of a sintered porous Ni–Cu alloy cathode for hydrogen production in a potassium hydroxide solution. *Energy* **2016**, *97*, 498–505. [[CrossRef](#)]
7. Wu, Y.; Lian, J.; Wang, Y.; Sun, J.; He, Z.; Gu, Z. Potentiostatic electrodeposition of self-supported NiS electrocatalyst supported on Ni foam for efficient hydrogen evolution. *Mater. Des.* **2021**, *198*, 109316. [[CrossRef](#)]
8. Suen, N.-T.; Hung, S.-F.; Quan, Q.; Zhang, N.; Xu, Y.-J.; Chen, H.M. Electrocatalysis for the oxygen evolution reaction: Recent development and future perspectives. *Chem. Soc. Rev.* **2017**, *46*, 337–365. [[CrossRef](#)]
9. Tian, X.; Zhao, X.; Su, Y.-Q.; Wang, L.; Wang, H.; Dang, D.; Chi, B.; Liu, H.; Hensen, E.J.; Lou, X.W. Engineering bunched Pt-Ni alloy nanocages for efficient oxygen reduction in practical fuel cells. *Science* **2019**, *366*, 850–856. [[CrossRef](#)]

10. Maeda, K.; Teramura, K.; Lu, D.; Takata, T.; Saito, N.; Inoue, Y.; Domen, K. Photocatalyst releasing hydrogen from water. *Nature* **2006**, *440*, 295. [[CrossRef](#)]
11. Tang, C.; Zhang, R.; Lu, W.; He, L.; Jiang, X.; Asiri, A.M.; Sun, X. Fe-doped CoP nanoarray: A monolithic multifunctional catalyst for highly efficient hydrogen generation. *Adv. Mater.* **2017**, *29*, 1602441. [[CrossRef](#)] [[PubMed](#)]
12. Ahmed, Z.; Ahmad, M.; Murshed, M.; Shah, M.I.; Mahmood, H.; Abbas, S. How do green energy technology investments, technological innovation, and trade globalization enhance green energy supply and stimulate environmental sustainability in the G7 countries? *Gondwana Res.* **2022**, *112*, 105–115. [[CrossRef](#)]
13. Santos, D.M.; Sequeira, C.A.; Figueiredo, J.L. Hydrogen production by alkaline water electrolysis. *Química Nova* **2013**, *36*, 1176–1193. [[CrossRef](#)]
14. Rashid, M.; Al Mesfer, M.K.; Naseem, H.; Danish, M. Hydrogen production by water electrolysis: A review of alkaline water electrolysis, PEM water electrolysis and high temperature water electrolysis. *Int. J. Eng. Adv. Technol.* **2015**, *4*, 80.
15. Hall, D. Electrodes for alkaline water electrolysis. *J. Electrochem. Soc.* **1981**, *128*, 740. [[CrossRef](#)]
16. Ma, S.; Sadakiyo, M.; Luo, R.; Heima, M.; Yamauchi, M.; Kenis, P.J. One-step electrosynthesis of ethylene and ethanol from CO₂ in an alkaline electrolyzer. *J. Power Sources* **2016**, *301*, 219–228. [[CrossRef](#)]
17. LeRoy, R. Industrial water electrolysis: Present and future. *Int. J. Hydrogen Energy* **1983**, *8*, 401–417. [[CrossRef](#)]
18. Fang, Y.-H.; Liu, Z.-P. Mechanism and tafel lines of electro-oxidation of water to oxygen on RuO₂ (110). *J. Am. Chem. Soc.* **2010**, *132*, 18214–18222. [[CrossRef](#)]
19. Zhao, M.; Wang, Y.; Ma, Q.; Huang, Y.; Zhang, X.; Ping, J.; Zhang, Z.; Lu, Q.; Yu, Y.; Xu, H. Ultrathin 2D metal–organic framework nanosheets. *Adv. Mater.* **2015**, *27*, 7372–7378. [[CrossRef](#)]
20. Ensafi, A.A.; Nabiyan, A.; Jafari-Asl, M.; Dinari, M.; Farokhpour, H.; Rezaei, B. Galvanic exchange at layered doubled hydroxide/N-doped graphene as an in-situ method to fabricate powerful electrocatalysts for hydrogen evolution reaction. *Energy* **2016**, *116*, 1087–1096. [[CrossRef](#)]
21. Lyons, M.E.; Brandon, M.P. The oxygen evolution reaction on passive oxide covered transition metal electrodes in aqueous alkaline solution. Part 1-Nickel. *Int. J. Electrochem. Sci.* **2008**, *3*, 1386–1424. [[CrossRef](#)]
22. Hall, D.S.; Lockwood, D.J.; Bock, C.; MacDougall, B.R. Nickel hydroxides and related materials: A review of their structures, synthesis and properties. *Proc. R. Soc. A Math. Phys. Eng. Sci.* **2015**, *471*, 20140792. [[CrossRef](#)] [[PubMed](#)]
23. Ishaq, H.; Dincer, I.; Crawford, C. A review on hydrogen production and utilization: Challenges and opportunities. *Int. J. Hydrogen Energy* **2022**, *47*, 26238–26264. [[CrossRef](#)]
24. Pareek, A.; Dom, R.; Gupta, J.; Chandran, J.; Adepu, V.; Borse, P.H. Insights into renewable hydrogen energy: Recent advances and prospects. *Mater. Sci. Energy Technol.* **2020**, *3*, 319–327. [[CrossRef](#)]
25. Zhou, D.; Li, P.; Xu, W.; Jawaid, S.; Mohammed-Ibrahim, J.; Liu, W.; Kuang, Y.; Sun, X. Recent advances in non-precious metal-based electrodes for alkaline water electrolysis. *ChemNanoMat* **2020**, *6*, 336–355. [[CrossRef](#)]
26. Liu, D.; Xu, H.; Wang, C.; Shang, H.; Yu, R.; Wang, Y.; Li, J.; Li, X.; Du, Y. 3D porous Ru-doped NiCo-MOF hollow nanospheres for boosting oxygen evolution reaction electrocatalysis. *Inorg. Chem.* **2021**, *60*, 5882–5889. [[CrossRef](#)] [[PubMed](#)]
27. Feng, J.X.; Xu, H.; Dong, Y.T.; Ye, S.H.; Tong, Y.X.; Li, G.R. FeOOH/Co/FeOOH hybrid nanotube arrays as high-performance electrocatalysts for the oxygen evolution reaction. *Angew. Chem. Int. Ed.* **2016**, *55*, 3694–3698. [[CrossRef](#)]
28. Tran, T.Q.N.; Das, G.; Yoon, H.H. Nickel-metal organic framework/MWCNT composite electrode for non-enzymatic urea detection. *Sens. Actuators B Chem.* **2017**, *243*, 78–83. [[CrossRef](#)]
29. Cheng, Y.; Xiao, X.; Guo, X.; Yao, H.; Pang, H. Synthesis of “Quasi-Ce-MOF” electrocatalysts for enhanced urea oxidation reaction performance. *ACS Sustain. Chem. Eng.* **2020**, *8*, 8675–8680. [[CrossRef](#)]
30. Amouzesh, S.P.; Khodadadi, A.A.; Mortazavi, Y.; Saris, S.; Asgari, M. MIL-100 (Fe)/ZnO nanocomposite sensors: An enhanced ammonia selectivity and low operating temperature. *Sens. Actuators B Chem.* **2024**, *399*, 134791. [[CrossRef](#)]
31. Bibi, S.; Pervaiz, E.; Ali, M. Synthesis and applications of metal oxide derivatives of ZIF-67: A mini-review. *Chem. Pap.* **2021**, *75*, 2253–2275. [[CrossRef](#)]
32. Zhang, S.; Luo, J.; Dai, L.; Zhou, S.; Tang, T.; Ai, S. NiCoP self-supporting electrode with the sea urchin-like microstructure for the synchronous reaction of hydrogen evolution and contaminant degradation. *J. Electroanal. Chem.* **2021**, *891*, 115273. [[CrossRef](#)]
33. Li, W.; Gao, X.; Wang, X.; Xiong, D.; Huang, P.-P.; Song, W.-G.; Bao, X.; Liu, L. From water reduction to oxidation: Janus Co-Ni-P nanowires as high-efficiency and ultrastable electrocatalysts for over 3000 h water splitting. *J. Power Sources* **2016**, *330*, 156–166. [[CrossRef](#)]
34. Li, L.; Li, X.; Ai, L.; Jiang, J. MOF-derived nanostructured cobalt phosphide assemblies for efficient hydrogen evolution reaction. *RSC Adv.* **2015**, *5*, 90265–90271. [[CrossRef](#)]
35. Zhou, X.; Xia, Z.; Zhang, Z.; Ma, Y.; Qu, Y. One-step synthesis of multi-walled carbon nanotubes/ultra-thin Ni(OH)₂ nanoplate composite as efficient catalysts for water oxidation. *J. Mater. Chem. A* **2014**, *2*, 11799–11806. [[CrossRef](#)]
36. Zhu, W.; Yue, X.; Zhang, W.; Yu, S.; Zhang, Y.; Wang, J.; Wang, J. Nickel sulfide microsphere film on Ni foam as an efficient bifunctional electrocatalyst for overall water splitting. *Chem. Commun.* **2016**, *52*, 1486–1489. [[CrossRef](#)]
37. Yu, X.-Y.; Feng, Y.; Guan, B.; Lou, X.W.D.; Paik, U. Carbon coated porous nickel phosphides nanoplates for highly efficient oxygen evolution reaction. *Energy Environ. Sci.* **2016**, *9*, 1246–1250. [[CrossRef](#)]
38. Thangasamy, P.; Shanmuganathan, S.; Subramanian, V. A NiCo-MOF nanosheet array based electrocatalyst for the oxygen evolution reaction. *Nanoscale Adv.* **2020**, *2*, 2073–2079. [[CrossRef](#)]

39. Guan, H.; Wang, N.; Feng, X.; Bian, S.; Liu, Y.; Ma, M.; Li, W.; Chen, Y. S element-doped synergistically well-mixed MOFs as highly efficient oxygen precipitation electrocatalyst. *Int. J. Hydrogen Energy* **2020**, *45*, 24333–24340. [[CrossRef](#)]
40. Dou, S.; Tao, L.; Wang, R.; El Hankari, S.; Chen, R.; Wang, S. Plasma-assisted synthesis and surface modification of electrode materials for renewable energy. *Adv. Mater.* **2018**, *30*, 1705850. [[CrossRef](#)]
41. Mistry, H.; Varela, A.S.; Bonifacio, C.S.; Zegkinoglou, I.; Sinev, I.; Choi, Y.-W.; Kisslinger, K.; Stach, E.A.; Yang, J.C.; Strasser, P. Highly selective plasma-activated copper catalysts for carbon dioxide reduction to ethylene. *Nat. Commun.* **2016**, *7*, 12123. [[CrossRef](#)] [[PubMed](#)]
42. Wang, Z.; Zhang, Y.; Neyts, E.C.; Cao, X.; Zhang, X.; Jang, B.W.-L.; Liu, C.-J. Catalyst preparation with plasmas: How does it work? *ACS Catal.* **2018**, *8*, 2093–2110. [[CrossRef](#)]
43. Yan, D.; Li, Y.; Huo, J.; Chen, R.; Dai, L.; Wang, S. Defect chemistry of nonprecious-metal electrocatalysts for oxygen reactions. *Adv. Mater.* **2017**, *29*, 1606459. [[CrossRef](#)]
44. Yu, Z.Y.; Duan, Y.; Feng, X.Y.; Yu, X.; Gao, M.R.; Yu, S.H. Clean and affordable hydrogen fuel from alkaline water splitting: Past, recent progress, and future prospects. *Adv. Mater.* **2021**, *33*, 2007100. [[CrossRef](#)] [[PubMed](#)]
45. Tao, L.; Duan, X.; Wang, C.; Duan, X.; Wang, S. Plasma-engineered MoS₂ thin-film as an efficient electrocatalyst for hydrogen evolution reaction. *Chem. Commun.* **2015**, *51*, 7470–7473. [[CrossRef](#)] [[PubMed](#)]
46. Zhang, T.; Wu, J.; Chen, J.; Pan, Q.; Wang, X.; Zhong, H.; Tao, R.; Yan, J.; Hu, Y.; Ye, X. Activating titanium metal with H₂ plasma for the hydrogen evolution reaction. *ACS Appl. Mater. Interfaces* **2021**, *13*, 24682–24691. [[CrossRef](#)] [[PubMed](#)]
47. Liu, C.; Tseng, C.-Y.; Wang, Y.-C.; Cheng, I.-C.; Chen, J.-Z. Low-Pressure Plasma-Processed Ruthenium/Nickel Foam Electrocatalysts for Hydrogen Evolution Reaction. *Materials* **2022**, *15*, 2603. [[CrossRef](#)]
48. Tseng, C.-Y.; Cheng, I.-C.; Chen, J.-Z. Low-pressure-plasma-processed NiFe-MOFs/nickel foam as an efficient electrocatalyst for oxygen evolution reaction. *Int. J. Hydrogen Energy* **2022**, *47*, 35990–35998. [[CrossRef](#)]
49. Xu, L.; Jiang, Q.; Xiao, Z.; Li, X.; Huo, J.; Wang, S.; Dai, L. Plasma-engraved Co₃O₄ nanosheets with oxygen vacancies and high surface area for the oxygen evolution reaction. *Angew. Chem.* **2016**, *128*, 5363–5367. [[CrossRef](#)]
50. Wang, Y.; Zhou, T.; Jiang, K.; Da, P.; Peng, Z.; Tang, J.; Kong, B.; Cai, W.B.; Yang, Z.; Zheng, G. Reduced mesoporous Co₃O₄ nanowires as efficient water oxidation electrocatalysts and supercapacitor electrodes. *Adv. Energy Mater.* **2014**, *4*, 1400696. [[CrossRef](#)]
51. Zhu, K.; Shi, F.; Zhu, X.; Yang, W. The roles of oxygen vacancies in electrocatalytic oxygen evolution reaction. *Nano Energy* **2020**, *73*, 104761. [[CrossRef](#)]
52. Lotfi, N.; Shahrabi, T.; Yaghoubinezhad, Y.; Darband, G.B. Electrodeposition of cedar leaf-like graphene Oxide@ Ni–Cu@ Ni foam electrode as a highly efficient and ultra-stable catalyst for hydrogen evolution reaction. *Electrochim. Acta* **2019**, *326*, 134949. [[CrossRef](#)]
53. Chen, D.; Liu, Z. Dual-axial gradient doping (Zr and Sn) on hematite for promoting charge separation in photoelectrochemical water splitting. *ChemSusChem* **2018**, *11*, 3438–3448. [[CrossRef](#)] [[PubMed](#)]
54. Fujimura, T.; Hikima, W.; Fukunaka, Y.; Homma, T. Analysis of the effect of surface wettability on hydrogen evolution reaction in water electrolysis using micro-patterned electrodes. *Electrochem. Commun.* **2019**, *101*, 43–46. [[CrossRef](#)]
55. Lu, Z.; Zhu, W.; Yu, X.; Zhang, H.; Li, Y.; Sun, X.; Wang, X.; Wang, H.; Wang, J.; Luo, J. Ultrahigh hydrogen evolution performance of under-water “superhydrophobic” MoS₂ nanostructured electrodes. *Adv. Mater.* **2014**, *26*, 2683–2687. [[CrossRef](#)] [[PubMed](#)]
56. Santos, D.; Šljukić, B.; Sequeira, C.; Macciò, D.; Saccone, A.; Figueiredo, J. Electrocatalytic approach for the efficiency increase of electrolytic hydrogen production: Proof-of-concept using platinum–dysprosium alloys. *Energy* **2013**, *50*, 486–492. [[CrossRef](#)]
57. Veeramani, V.; Madhu, R.; Chen, S.-M.; Sivakumar, M.; Hung, C.-T.; Miyamoto, N.; Liu, S.-B. NiCo₂O₄-decorated porous carbon nanosheets for high-performance supercapacitors. *Electrochim. Acta* **2017**, *247*, 288–295. [[CrossRef](#)]
58. Chen, Q.; Lei, S.; Deng, P.; Ou, X.; Chen, L.; Wang, W.; Xiao, Y.; Cheng, B. Direct growth of nickel terephthalate on Ni foam with large mass-loading for high-performance supercapacitors. *J. Mater. Chem. A* **2017**, *5*, 19323–19332. [[CrossRef](#)]
59. Gopalakrishnan, M.; Mohamad, A.; Nguyen, M.; Yonezawa, T.; Qin, J.; Thamyongkit, P.; Somwangthana, A.; Kheawhom, S. Recent advances in oxygen electrocatalysts based on tunable structural polymers. *Mater. Today Chem.* **2022**, *23*, 100632. [[CrossRef](#)]
60. Liang, Q.; Chen, J.; Wang, F.; Li, Y. Transition metal-based metal-organic frameworks for oxygen evolution reaction. *Coord. Chem. Rev.* **2020**, *424*, 213488. [[CrossRef](#)]
61. Tahir, M.; Pan, L.; Idrees, F.; Zhang, X.; Wang, L.; Zou, J.-J.; Wang, Z.L. Electrocatalytic oxygen evolution reaction for energy conversion and storage: A comprehensive review. *Nano Energy* **2017**, *37*, 136–157. [[CrossRef](#)]
62. Fu, H.Q.; Zhou, M.; Liu, P.F.; Liu, P.; Yin, H.; Sun, K.Z.; Yang, H.G.; Al-Mamun, M.; Hu, P.; Wang, H.-F. Hydrogen spillover-bridged Volmer/Tafel processes enabling ampere-level current density alkaline hydrogen evolution reaction under low overpotential. *J. Am. Chem. Soc.* **2022**, *144*, 6028–6039. [[CrossRef](#)] [[PubMed](#)]
63. Dai, Z.; Du, X.; Zhang, X. Controlled synthesis of NiCo₂O₄@ Ni-MOF on Ni foam as efficient electrocatalyst for urea oxidation reaction and oxygen evolution reaction. *Int. J. Hydrogen Energy* **2022**, *47*, 17252–17262. [[CrossRef](#)]
64. Kapałka, A.; Fóti, G.; Comninellis, C. Determination of the Tafel slope for oxygen evolution on boron-doped diamond electrodes. *Electrochem. Commun.* **2008**, *10*, 607–610. [[CrossRef](#)]
65. Shinagawa, T.; Garcia-Esparza, A.T.; Takanabe, K. Insight on Tafel slopes from a microkinetic analysis of aqueous electrocatalysis for energy conversion. *Sci. Rep.* **2015**, *5*, 13801. [[CrossRef](#)] [[PubMed](#)]

66. Zhang, Y.; Cui, W.; Li, L.; Zhan, C.; Xiao, F.; Quan, X. Effect of aligned porous electrode thickness and pore size on bubble removal capability and hydrogen evolution reaction performance. *J. Power Sources* **2023**, *580*, 233380. [[CrossRef](#)]
67. Wu, L.; He, Y.; Lei, T.; Nan, B.; Xu, N.; Zou, J.; Huang, B.; Liu, C. Characterization of the porous Ni₃Al–Mo electrodes during hydrogen generation from alkaline water electrolysis. *Energy* **2013**, *63*, 216–224. [[CrossRef](#)]
68. Li, D.; Xu, Y.; Lu, Y.; Chen, Y.; Wu, Y.; Yan, J.; Du, F.; Zhao, Y.; Tan, X. Defect-rich engineering of Ni-incorporated tungsten oxides micro-flowers on carbon cloth: A binder-free electrode for highly efficient hydrogen evolution reaction. *J. Power Sources* **2022**, *520*, 230862. [[CrossRef](#)]
69. Shervedani, R.K.; Madram, A.R. Kinetics of hydrogen evolution reaction on nanocrystalline electrodeposited Ni₆₂Fe₃₅C₃ cathode in alkaline solution by electrochemical impedance spectroscopy. *Electrochim. Acta* **2007**, *53*, 426–433. [[CrossRef](#)]
70. Cossar, E.; Houache, M.S.; Zhang, Z.; Baranova, E.A. Comparison of electrochemical active surface area methods for various nickel nanostructures. *J. Electroanal. Chem.* **2020**, *870*, 114246. [[CrossRef](#)]
71. Yang, Y.; Zhang, W.; Xiao, Y.; Shi, Z.; Cao, X.; Tang, Y.; Gao, Q. CoNiSe₂ heteronanorods decorated with layered-double-hydroxides for efficient hydrogen evolution. *Appl. Catal. B Environ.* **2019**, *242*, 132–139. [[CrossRef](#)]
72. Zhao, Z.; Wu, H.; Li, C. Engineering iron phosphide-on-plasmonic Ag/Au-nanoshells as an efficient cathode catalyst in water splitting for hydrogen production. *Energy* **2021**, *218*, 119520. [[CrossRef](#)]
73. Liang, H.; Alshareef, H.N. A plasma-assisted route to the rapid preparation of transition-metal phosphides for energy conversion and storage. *Small Methods* **2017**, *1*, 1700111. [[CrossRef](#)]
74. Choi, E.Y.; Moon, S.H. Characterization of acrylic acid-grafted PP membranes prepared by plasma-induced graft polymerization. *J. Appl. Polym. Sci.* **2007**, *105*, 2314–2320. [[CrossRef](#)]
75. Staño, L.; Stano, M.; Đurina, P. Separators for alkaline water electrolysis prepared by plasma-initiated grafting of acrylic acid on microporous polypropylene membranes. *Int. J. Hydrogen Energy* **2020**, *45*, 80–93. [[CrossRef](#)]
76. Detsi, E.; Cook, J.B.; Lesel, B.K.; Turner, C.L.; Liang, Y.-L.; Robbennolt, S.; Tolbert, S.H. Mesoporous Ni₆Fe₃₀Mn₁₀-alloy based metal/metal oxide composite thick films as highly active and robust oxygen evolution catalysts. *Energy Environ. Sci.* **2016**, *9*, 540–549. [[CrossRef](#)]
77. Yin, H.; Zhao, S.; Zhao, K.; Muqsit, A.; Tang, H.; Chang, L.; Zhao, H.; Gao, Y.; Tang, Z. Ultrathin platinum nanowires grown on single-layered nickel hydroxide with high hydrogen evolution activity. *Nat. Commun.* **2015**, *6*, 6430. [[CrossRef](#)]
78. Balogun, M.S.; Qiu, W.; Huang, Y.; Yang, H.; Xu, R.; Zhao, W.; Li, G.R.; Ji, H.; Tong, Y. Cost-Effective Alkaline Water Electrolysis Based on Nitrogen-and Phosphorus-Doped Self-Supportive Electrocatalysts. *Adv. Mater.* **2017**, *29*, 1702095. [[CrossRef](#)]
79. Niyitanga, T.; Kim, H. Bimetallic-based Cu_xCo_{3-x}O₄ nanoparticle-embedded N-doped reduced graphene oxide toward efficient oxygen evolution reaction and hydrogen evolution reaction for bifunctional catalysis. *J. Power Sources* **2023**, *580*, 233383. [[CrossRef](#)]
80. Osmieri, L.; He, Y.; Chung, H.T.; McCool, G.; Zulevi, B.; Cullen, D.A.; Zelenay, P. La–Sr–Co oxide catalysts for oxygen evolution reaction in anion exchange membrane water electrolyzer: The role of electrode fabrication on performance and durability. *J. Power Sources* **2023**, *556*, 232484. [[CrossRef](#)]
81. Shen, X.; Zhang, X.; Li, G.; Lie, T.T.; Hong, L. Experimental study on the external electrical thermal and dynamic power characteristics of alkaline water electrolyzer. *Int. J. Energy Res.* **2018**, *42*, 3244–3257. [[CrossRef](#)]
82. Mohammadi, A.; Mehrpooya, M. A comprehensive review on coupling different types of electrolyzer to renewable energy sources. *Energy* **2018**, *158*, 632–655. [[CrossRef](#)]
83. Gilliam, R.; Graydon, J.; Kirk, D.; Thorpe, S. A review of specific conductivities of potassium hydroxide solutions for various concentrations and temperatures. *Int. J. Hydrogen Energy* **2007**, *32*, 359–364. [[CrossRef](#)]
84. Kothari, R.; Buddhi, D.; Sawhney, R. Studies on the effect of temperature of the electrolytes on the rate of production of hydrogen. *Int. J. Hydrogen Energy* **2005**, *30*, 261–263. [[CrossRef](#)]
85. Diéguez, P.; Ursúa, A.; Sanchis, P.; Sopena, C.; Guelbenzu, E.; Gandía, L. Thermal performance of a commercial alkaline water electrolyzer: Experimental study and mathematical modeling. *Int. J. Hydrogen Energy* **2008**, *33*, 7338–7354. [[CrossRef](#)]
86. Shin, Y.; Park, W.; Chang, J.; Park, J. Evaluation of the high temperature electrolysis of steam to produce hydrogen. *Int. J. Hydrogen Energy* **2007**, *32*, 1486–1491. [[CrossRef](#)]
87. Haynes, W.M. *CRC Handbook of Chemistry and Physics*; CRC Press: Boca Raton, FL, USA, 2014.

Disclaimer/Publisher’s Note: The statements, opinions and data contained in all publications are solely those of the individual author(s) and contributor(s) and not of MDPI and/or the editor(s). MDPI and/or the editor(s) disclaim responsibility for any injury to people or property resulting from any ideas, methods, instructions or products referred to in the content.